Journal of Superconductivity and Novel Magnetism (2022) 35:2923–2932
https://doi.org/10.1007/s10948-022-06281-x

ORIGINAL PAPER

Microstructure, Exchange Interaction and Magnetic Properties of Nanocrystalline Zr_6Co_{23}/MgO(001) Films

R. Fersi[1] · A. P. Dalia[2]

Received: 8 January 2022 / Accepted: 4 May 2022 / Published online: 8 July 2022
© Springer Science+Business Media, LLC, part of Springer Nature 2022

Abstract
In this work, we have studied the effect of thickness δ on the microstructural and magnetic properties of nanocrystalline Zr_6Co_{23} films grown on MgO(001) substrate. A series of Zr_6Co_{23}/MgO(001) films have been prepared for different thickness δ. The coercivity H_c, the squareness factor S* and the anisotropy field H_a are investigated as a function of δ thickness and grain sizes Φ. The excellent magnetic properties are found for $\delta = 100$ nm: the coercivity $H_c = 3020$ Oe, maximum energy product $(BH)_{max}$ of 28 MGOe and magnetic anisotropy constant $K_1 \simeq 1.35 \times 10^7$ erg/cm^3. The relationships between exchange interaction, magnetic domain structure and anisotropy parameters are discussed. The obtained results provide the fundamental reference to adapt the magnetic properties of Zr_6Co_{23}/MgO(001) films for potential applications in the permanent magnet domain.

Keywords Nanocrystalline Zr_6Co_{23}/MgO(001) film · Microstructure properties · Magnetic properties

1 Introduction

The development of thin films based on Co alloys is of major interest in industrial application fields [1–3].Their important magnetic properties thus give them use in permanent magnets, magnetic recording high density and spintronic devices [4–6]. Among these alloys, ZrCo alloys exhibit a high coercivity H_C and magnetocrystalline anisotropy H_a. These properties place them among the best performing magnetic materials [7–10]. In the binary Zr-Co system, several compounds are formed: ZrCo, Zr_2Co, Zr_3Co, $ZrCo_5$, Zr_2Co_{11}, $ZrCo_2$, Zr_4Co, Zr_6Co_{23} and Zr_3Co_2 which have quite diverse structural and magnetic properties [12–14] ZrCo type of magnets are known an industrial and technological scale mainly under three stoichiometries: $ZrCo_5$, Zr_2Co_{11} and Zr_6Co_{23}, which have very important magnetic properties related to 3d-3d hybridization and 3d-3d exchange interactions [15–17]. Burzo et al. [13, 18, 19] reported that the $ZrCo_5$ compound exhibits ferromagnetic behavior with uniaxial anisotropy greater than 99902 Oe and the Curie temperature T_C is around 800 Gabay et al. [13, 14, 18] found a H_c of 2488 Oe and a maximum energy product $(BH)_{max}$ of 10.1 MGOe for $Zr_{16.4}Co_{83.6}$ (Zr_2Co_{11}) compound produced arc melting. The magnetic anisotropy $H_a = 9927$ Oe and the Curie temperature $T_C = 773$ Saito et al. [8, 9] studied the magnetic properties of $Zr_{18}Co_{80}B_2$ melt-spun ribbons. The $(BH)_{max} = 46.5$ MGOe and $H_c = 5026$ Oe, consecutively. The Zr_2Co_{11}/Si(100) films (for thickness $\delta = 1$ nm) have a high $H_c = 3041$ Oe and $(BH)_{max} \simeq 24$ MGOe [20]. The best magnetic properties of $ZrCo_5$/MgO(100) film are found for thickness $\delta = 40$ nm [21]. The H_c is around 65 Oe, $(BH)_{max} \simeq 9.4$ MGOe and uniaxial anisotropy constant $K_u \simeq 7.8 \times 10^5$ erg/cm^3. The Zr_6Co_{23} alloy presents fascinating magnetic properties. The Curie temperature T_C of 766 K, saturation polarization $J_s \simeq 25132$ Oe and $H_a = 101159$ Oe [10, 11]. The interesting obtained results suggest that films of Zr_6Co_{23} compound can also have excellent magnetic properties. The preparation of these films with different thicknesses can result in varying surface morphology (island/grain size, roughness), domain patterns, magnetic anisotropies that can significantly influence the overall magnetic properties and magnetization reversal mechanism of films. In this context, in the present work, a detailed study has been undertaken to understand the structure, surface morphology, magnetic microstructure and magnetic properties of Zr_6Co_{23} films over a wide range of thicknesses.

✉ R. Fersi
riadh.fersi@fst.utm.tn

[1] Laboratoire Matériaux Organisation et Propriétés (LR99ES17), Faculté des Sciences de Tunis, Université de Tunis El Manar, Tunis 2092, Tunisia

[2] Department of Materials Science and Engineering, 313 Splaiul Unirii Street, 020745 Bucharest, Romania

The Zr_6Co_{23} films were prepared by Pulsed Laser Deposition (PLD) on MgO(001) substrate. The influence of thickness δ on microstructure and magnetic properties was investigated. The relationships between morphology, exchange interaction and magnetic anisotropy properties are discussed. We optimized the microstructure of Zr_6Co_{23}/MgO(001) films in order to find high extrinsic magnetic properties.

2 Experimental Procedures

2.1 Nanocrystalline Zr_6Co_{23}/MgO(001) Film Preparation

Zr_6Co_{23}/MgO(001) films were prepared by Pulsed Laser Deposition (PLD) from nanocrystalline Zr_6Co_{23} powder, using a Nd:YAG laser with wavelength $\lambda = 535$ nm, repetition rate of 10 Hz and max pulse energy of 2×10^8 J [22, 23]. The nanocrystalline Zr_6Co_{23} powder was prepared by mechanical alloying method for 72 h of milling time (Sect. 3.1). Before deposition, the Zr_6Co_{23} target (Zr: Zirconium, Co: Cobalt, purity: 99.999 %) was ablated for 40 s to remove the contaminations. During deposition, the laser beam was at 45° incidence on the Zr_6Co_{23} target. The Zr_6Co_{23} target and the MgO(001) substrate were rotated for uniform ablation and homogeneous deposition. Eight samples of Zr_6Co_{23} films were deposited on [1mm × 0.5 mm] MgO(001) substrate wafers using several laser shots from 1500 to 6000, by ablating the laser beam on Zr_6Co_{23} target at deposition temperature 673 K. The thickness of Zr_6Co_{23} layer was 10, 50, 100, 150, 200, 250, 300 and 400 nm. After deposition, a 20 nm thick Au overlay layer was deposited on the top of Zr_6Co_{23} films to avoid oxidation. The growth parameters during the Pulsed Laser Deposition (PLD) are summarized in Table 1.

Table 1 Growth parameters of pulsed laser deposition (PLD)

Parameters	
Target	Zr_6Co_{23} (dimension: 5×10^{-2} m (diameter) and 3×10^{-2} m (thickness)
Substrate	[1mm × 0.5 mm] MgO(001)
Overlay layer(δ thickness)	Au(δ = 20 nm)
Laser fluence	2 J.cm^2
Substrate temperature	673 K
Gas used	High purity oxygen (99.7%)
Oxygen partial pressure	30×10^{-6} Pascal
Deposition time(X thickness)	15 min (10 nm), 32 min (50 nm)
	65 min (100 nm), 90 min (150 nm)
	120 min (200 nm), 150 min (250 nm)
	175 min (300 nm), 195 min (400 nm)

2.2 Microstructure and Magnetic Characterizations

The microstructural characterizations of Zr_6Co_{23}/MgO(001) film were analyzed by grazing incidence X-ray diffraction (GIXRD) technique. The surface morphologies, chemical compositions and cross-sectional images were detected by Field Emission Scanning Electron Microscope (FESEM) equipped energy-dispersive spectrometer (SEM-EDS). High-resolution transmission electron microscopy (HRTEM) imaging was performed using Tecnai G20 TEM. Atomic force microscopy (AFM, 3SPA-300HV) was employed to characterize the surface roughness (R_{rms}) and grain size (Φ) of films. The magnetic properties are investigated using a superconducting quantum interference device (SQUID) magnetometer Quantum Design MPM-SXL, vibrating sample magnetometer (VSM, BHV-525) and magnetic force microscopy (MFM).

3 Results and Discussion

3.1 Microstructure and Magnetic Properties of Nanocrystalline Zr_6Co_{23} Powders

The nanocrystalline Zr_6Co_{23} powders were prepared by high-energy ball milling [24, 25]. After milling for 5 hours with ball to powder ratio of 15/1, under high purity Ar atmosphere, the Zr_6Co_{23} samples, enveloped in tantalum foil, were annealed for 72 h in sealed silica tube under 10^{-6} Torr at several annealing temperature T_a from 600 K to 1750 K. The crystal structure of Zr_6Co_{23} sample was detected by X-ray diffraction (XRD) with CuK_α radiation. The pattern refinement was performed with the FULLPROF computing code based on the Rietveld technique [26–28]. The goodness-of-fit parameters χ^2 and R_B were used as numerical criteria to describe the quality of the fit between calculated and experimental XRD data [29–31]. Zr_6Co_{23} powders annealed at 1173 K. The result of the structure refinement shows the presence of a main phase with the cubic Th_6Mn_{23} type structure (Fm-3m space group (No.225)). We note minor quantities of the oxide phases appearing due to selective oxidation of ZrO_2 and Zr_6O. The lattice parameters are $a = b = c = 8.2662$ Å. The Zr atoms occupy the crystallographic 24e sites while Co atoms occupy two 32f sites, 24d and 4e sites. The lattice parameters, R_a and χ^2 factors from Rietveld fit are given in Table 2. These values of structural parameters are in agreement with the results obtained previously [32, 33]. The T_C temperature of Zr_6Co_{23} compound was determined from the M(T) curve by extrapolating the linear part of the M(T) curve and finding the temperature value of the intersection with the extended baseline [34, 35] (Fig. 1(b)). The T_C temperature

Table 2 a, b and c unit cell parameters, atomic positions, R_B and χ^2 factors, from Rietveld refinement of Zr_6Co_{23} compound annealed at $T_a = 1173$ K

Cell parameters	$a = b = c = 8.2662$ Å
Sites	Atomic positions (x, y, z)
Zr_1(24e)	(0.295, 0, 0)
Co_1(32f)	(0.122, 0.122, 0.122)
Co_2(32f)	(0.322, 0.322, 0.322)
Co_3(24d)	(0, 1/4, 1/4)
Co_4(4a)	(0, 0, 0)
R_B	3.25
χ^2	2.76

is around 768 K. In order to study the extrinsic properties, we have optimized the Zr_6Co_{23} microstructure, which can lead us to the best coercivity H_c. We have therefore used, for this compound, several annealing at different temperatures T_a. The optimum extrinsic magnetic properties are obtained for $T_a = 1173$ K: $H_c = 10172$ Oe, $M_r = 50.12$ emu/g and $(BH)_{max} = 50.73$ MGOe. Figure 2 shows the hysteresis loop at 298 K, for the nanocrystalline Zr_6Co_{23} sample annealed at 1173 K.

3.2 Microstructure Properties of Nanocrystalline Zr_6Co_{23}/MgO(001) Films

Figure 3 illustrates the GIXRD patterns of Zr_6Co_{23}/MgO(001) films deposited at 673 K for different thickness: $\delta = 10$ nm, 100 nm, 200 nm and 400 nm. The peak at $2\theta = 44.37°$ and 69.48° corresponds to (4 4 0) and (6 6 0) reflections, consecutively, indexed as cubic structure Th_6Mn_{23} type with Fm-3m space group [10]. The identification of the obtained peaks was made by assigning Miller indices (hkl) to the various recorded peaks using the Bragg condition and X'Pert high score database [36]. The majority of diffraction peaks of the films for $\delta < 400$ nm correspond to plane families (h k 0). For $\delta = 400$ nm, the appearance of peaks at $2\theta = 37.20°$ and 66.7° corresponds to Zr_6Co_{23}(4 4 2) and Zr_6Co_{23}(7 3 3) reflection can be seen. The additional peak at $2\theta = 39.7°$ and 45.5° corresponds to Au(1 1 1) and MgO(0 0 1) reflections, consecutively. The grains size Φ is evaluated from Scherrer's formula [37–39]: $\Phi = \kappa\ \lambda/(\beta_L.\mathrm{Cos}\theta)$, where β_L is the full-width at half-maximum (FWHM) of the peaks at the diffraction angle θ [29, 40, 41]. κ is the shape factor, equal to 0.9 in the present study. The calculation of the FWHM has been achieved for all films considering the most intense peak (4 4 0) at $2\theta = 44.37°$. The average grain size Φ is around 14 nm , 17 nm , 40 nm , 76 nm , 110 nm , 178 nm, 201 nm and 232 nm for thickness: $\delta = 20$ nm , $\delta = 50$ nm , $\delta = 100$ nm, $\delta = 150$ nm, $\delta = 200$ nm, $\delta = 250$ nm, $\delta = 300$ nm and $\delta = 400$ nm, consecutively (Table 4).

Figure 4 shows the cross-sectional STEM HAADF micrograph of Zr_6Co_{23}/MgO(001) films for $\delta = 10$ nm (a), 100 nm (b) and 400 nm (c). The boundary MgO/Zr_6Co_{23} and Zr_6Co_{23} /Au interfaces between the different layers: MgO, Zr_6Co_{23}, and Au are clearly seen. ESEM micrographs illustrate typical overviews of granular morphology of each sample (Fig. 4(a*, b*, c*)). Figure 5(a) presents the energy-dispersive x-ray spectroscopy (EDS) data analysis of Zr_6Co_{23} layers. EDS analysis was performed by scanning field emission electron microscopy (FESEM). The atomic percentage of Zr and Co, was 20.7 % and 79.3 %, consecutively (Fig. 5(a)). The stoichiometric proportions of Zr_6Co_{23} were roughly maintained. An EDX line profile was carried through between the grains (Fig. 5(c)), presenting the intensity distribution profiles of the Zr, Co and O elements. The black line corresponds to the

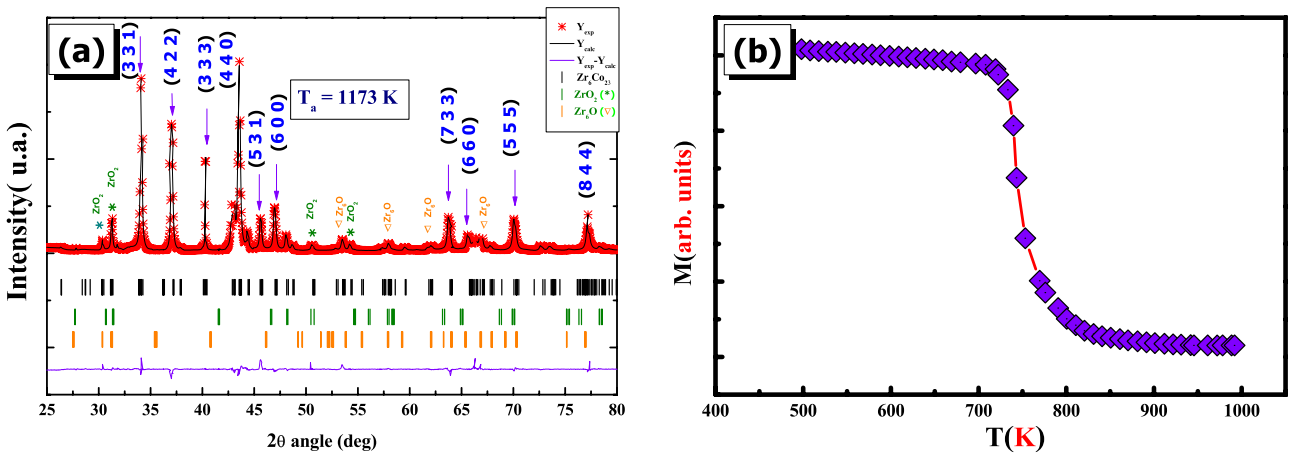

Fig. 1 **a** Rietveld analysis for X-ray diffraction patterns and **b** magnetization curve M(T) of nanocrystalline Zr_6Co_{23} compound annealed at $T_a = 1173$ K

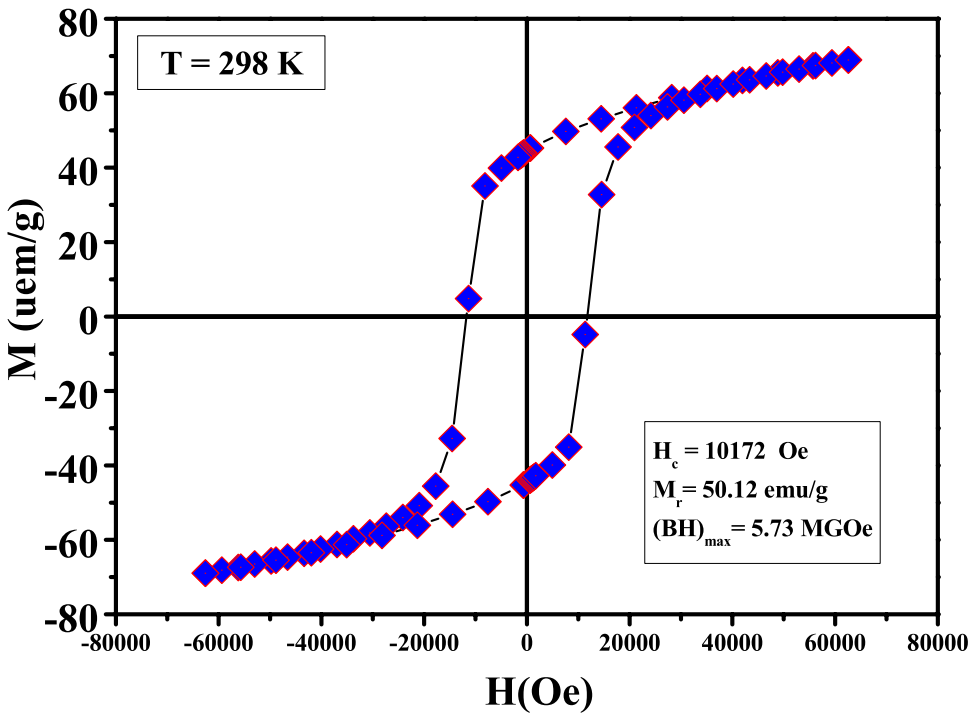

Fig. 2 Hysteresis loop of nanocrystalline Zr_6Co_{23} compound annealed at $T_a = 1173$ K, measured at 298 K

Zr profile, the red line to Co. The O is plotted using a blue line (Fig. 5(b)). A slight diminution of Zr intensity between the grains indicates a phase richer in O. Elemental maps carried on the location shown in Fig. 5(d), (e) and (f) confirm a O enrichment in the area in between the large grains. The appearance of oxygen in the films is due to the residual oxygen used during the deposition. We note the presence of some traces of impurities (C, Si and Ni) with low atomic percentage. The atomic compositions obtained by EDX analysis for different thickness δ are summarized in Table 3.

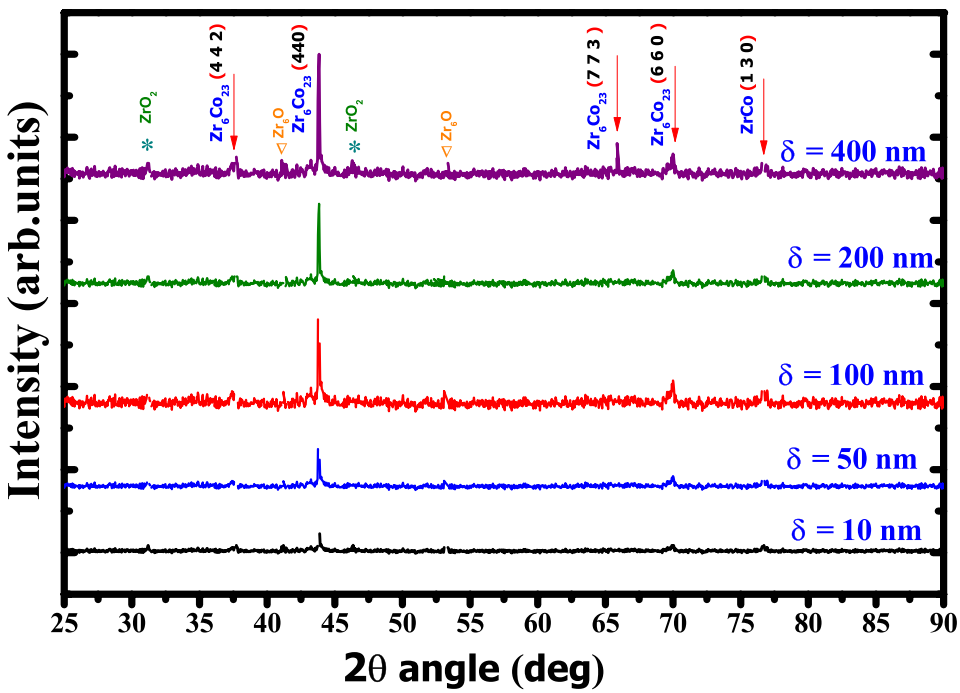

Fig. 3 GIXRD patterns for nanocrystalline Zr_6Co_{23}/MgO(001) films with different thickness: $\delta = 10$ nm, 100 nm, 200 nm and 400 nm

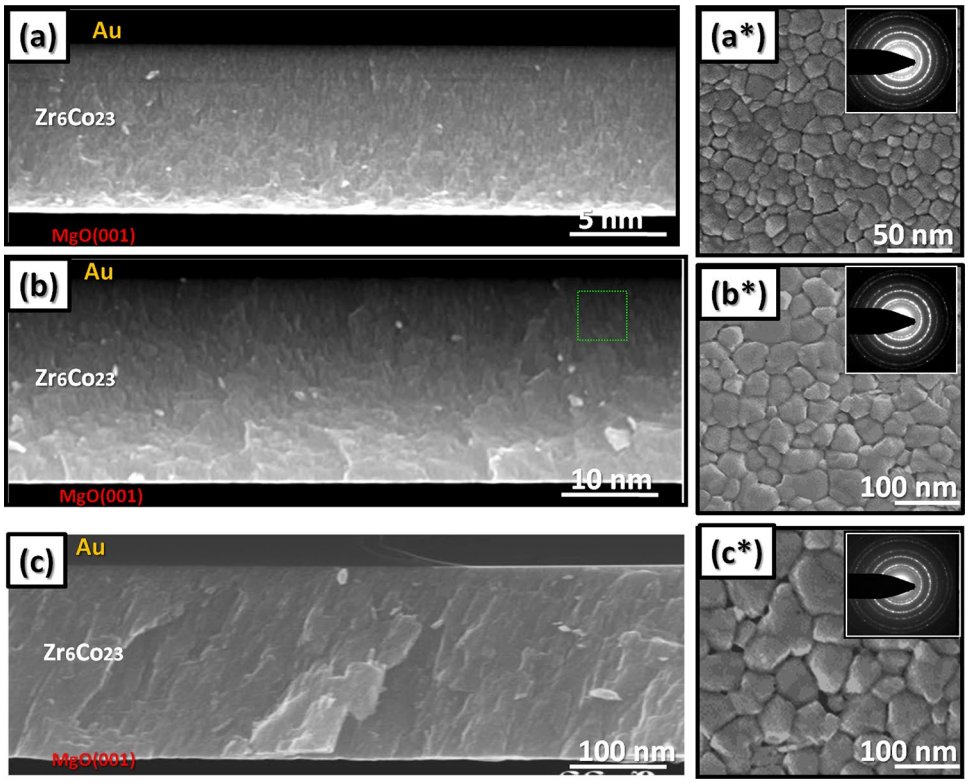

Fig. 4 Cross section SEM HAADF micrograph of nanocrystalline Zr_6Co_{23}/MgO(001) films for thickness: $\delta = 10$ nm (**a**), 100 nm (**b**) and 400 nm (**c**). ESEM micrographs of nanocrystalline Zr_6Co_{23}/MgO(001) films for thickness: $\delta = 10$ nm (**a***), 100 nm (**b***) and 400 nm (**c***). The corresponding selected area electron diffraction (SAED) patterns are presented in the inset

By making a statistic on the grain size, the grain size distribution of thickness: $\delta = 10$ nm, 100 nm and 400 nm is illustrated in Fig. 6. The average grain size Φ_{TEM} was estimated to be 15 nm, 35 nm and 230 nm, consecutively. The

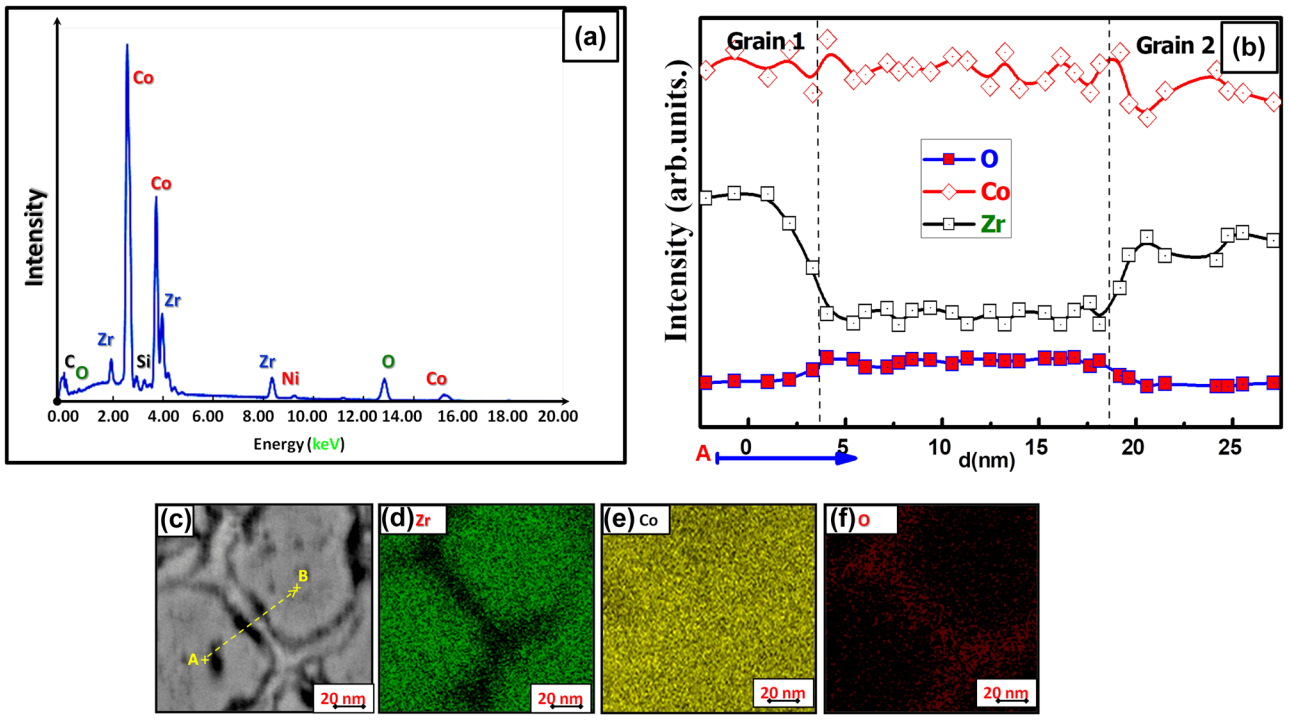

Fig. 5 **a** Energy-Dispersive X-ray Spectroscopy (EDS) data analysis of nanocrystalline Zr_6Co_{23} layers. **b** Scanning Transmission Electron Microscopy Energy-dispersive X-ray (STEM-EDX) mapping for $\delta = 100$ nm

Table 3 Atomic compositions of Zr_6Co_{23}/MgO(001) films obtained through EDX analysis: Zirconium (Zr), Cobalt (Co) and Oxygen (O)

δ(nm)	Zr(%. at)	Co(%. at)	O(%. at)
10	20	78	2
50	20.7	78.80	1.3
100	20.7	78	1.12
150	20	78.80	0.53
200	20.66	78.80	0.54
250	20.67	78.78	0.55
300	20.67	78	1.35
400	20.56	78.67	0.77

corresponding selected area electron diffraction (SAED) patterns are presented in the inset; it exhibits brilliant diffraction rings, which is a typical characteristic of nanocrystalline phase.

The surface topography images were obtained from the atomic force microscope (AFM) used as a source of information on root-mean-square roughness R_{rms} and grain size Φ [42]. Figure 7 shows (2D) AFM images of Zr_6Co_{23}/MgO(001) films as a function of δ thickness, over an area of 500 nm × 500 nm. The grains were evenly distributed over the surface of the substrate. The grain size estimation Φ in each case was given in the respective figures. The found values of Φ are in good agreement with the results obtained by GIXRD and TEM analysis. The surface roughness can be quantitatively defined by the root-mean-square roughness R_{rms} given by [43]:

$$R_{rms} = \sqrt{\frac{\sum_{n=1}^{N}(h_n - \hbar_n)^2}{N-1}} \quad (1)$$

where h_n represents the height of particle number n, $\hbar$ is the average of the heights h_n and N is the total number of particles measured by AFM [44]. The variation of R_{rms} as a function of δ thickness is shown in Table 4.

3.3 Magnetic Properties of Nanocrystalline Zr_6Co_{23}/MgO(001) Films

The hysteresis loops of Zr_6Co_{23}/MgO(001) film for different δ thickness are given in Fig. 8. We extracted the extrinsic magnetic properties. The evolution of the coercivity H_c, the maximum energy product $(BH)_{max}$, the remanent magnetization M_r and the squareness factor S* were investigated as a function of δ thickness and grain size Φ. Table 5 summarizes the evolution of H_c, M_r and $(BH)_{max}$ as

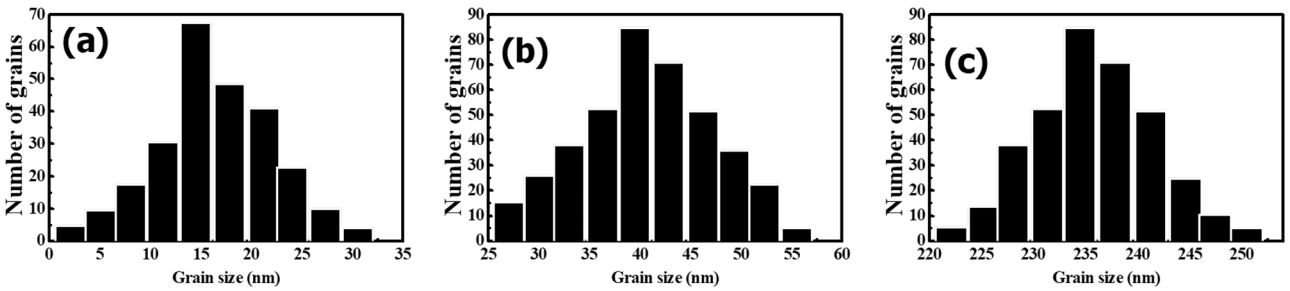

Fig. 6 The size distribution histograms for thickness: $\delta = 10$ nm (**a**), $\delta = 100$ nm (**b**) and 400 nm (**c**)

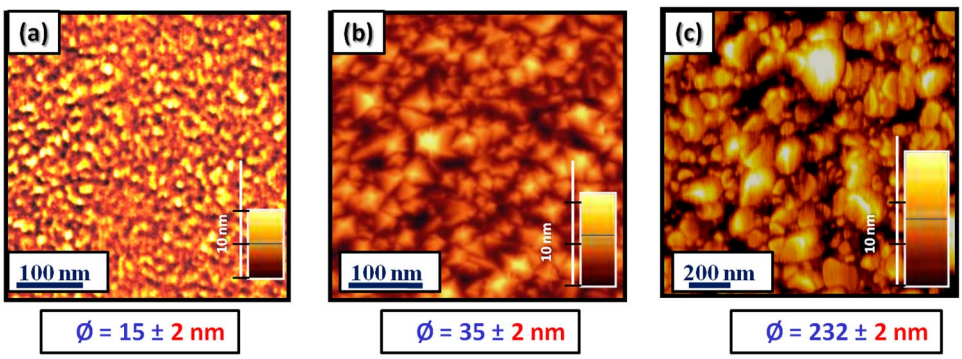

Fig. 7 AFM topographic images for nanocrystalline Zr_6Co_{23}/MgO(001) films with different thicknesses: $\delta = 10$ nm (**a**) , $\delta = 100$ nm (**b**) and $\delta = 400$ nm (**c**). The estimated grain size values Φ in each case are given in the respective figures

Table 4 The grain size Φ, roughness R_{rms} of nanocrystalline Zr_6Co_{23}/MgO(001) films for different δ thickness

δ(nm)	10	50	100	150	200	250	300	400
Φ(±2 nm)	14	17	40	76	110	178	201	232
R_{rms}(±0.2 nm)	5.92	6.14	6.26	6.73	7.79	8.15	10.42	11.51

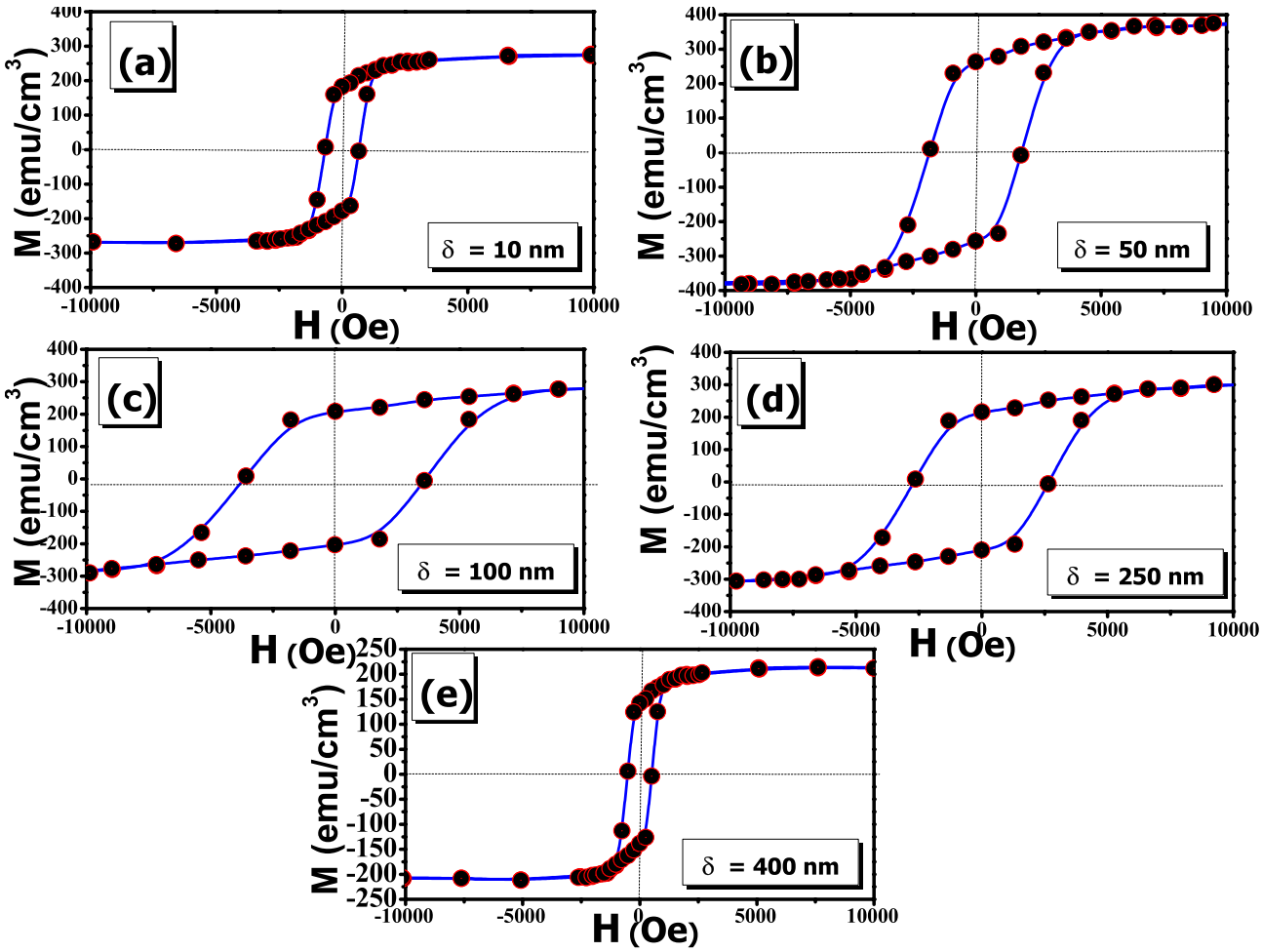

Fig. 8 Hysteresis loops of Zr_6Co_{23}/MgO(001) film for different δ thickness

Table 5 Coercivity H_c(Oe), maximum energy product $(BH)_{max}$(MGOe) and remanent magnetization M_r(emu/cm^3) of Zr_6Co_{23}/MgO(001) film for different δ thickness

δ(nm)	10	50	100	150	200	250	300	400
H_c(±0.3 Oe)	563	1193	3020	3003	2236	1355	1087	513
M_r(±0.3 emu/cm^3)	193	263	222	195	220	190	143	140
$(BH)_{max}$(±0.2 MGOe)	15	16	28	19	17	14	12	8

a function of δ thickness. The H_c increases with the thickness $\delta < 100$ nm. Then, a monotonous decrease of H_c was observed from 3020 Oe for $\delta = 100$ nm to 513 Oe for $\delta = 400$ nm. The high extrinsic magnetic properties were obtained for $\delta = 100$ nm: $H_c = 3020$ Oe, $M_r = 222$ emu/cm^3 and $(BH)_{max} = 28$ MGOe. The small H_c and $(BH)_{max}$ for thickness $\delta = 400$ nm due to an unfavorable microstructure related to the large grain size $\Phi \simeq 232$ nm. The H_c variation as a function of Φ can be described by $H_c(1/\Phi)$ [45, 46]. The critical grain size (Φ_c) from single domain to

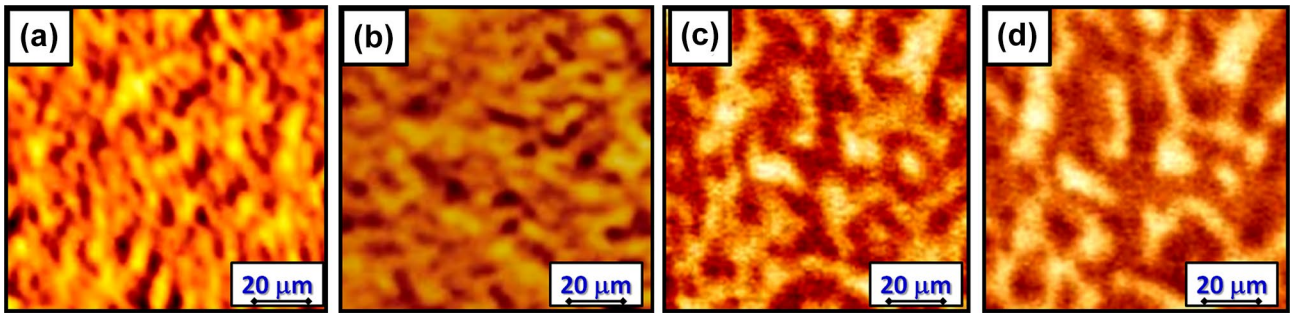

Fig. 9 MFM images of nanocrystalline Zr_6Co_{23}/MgO(001) films for $\delta = 10$ nm (**a**), $\delta = 100$ nm (**b**), $\delta = 300$ nm (**c**) and $\delta = 400$ nm (**d**)

multi-domain can be determined from the following formula [47]:

$$\Phi_c = 9\kappa/2\pi M_s^2 \tag{2}$$

where $\kappa = (2k_B.K_1.T_C/\rho)^{1/2}$ is the domain wall energy. k_B is Boltzmann constant, K_1 is anisotropy constant, T_C is Curie temperature, ρ is the lattice coefficient. The value obtained of Φ_c from formula (2) is around 41.5 nm. This result is in good agreement with the experimental value ($\Phi_c = 40 \pm 2$ nm) for Zr_6Co_{23}/MgO(001) ($\delta = 100$ nm) films. MFM is becoming one of the most used techniques for imaging magnetic domains [48]. Figure 9 presents the topographic MFM images of Zr_6Co_{23}/MgO(001) films for $\delta = 10$ nm, 100 nm, 300 nm and 400 nm. The MFM images show that the films surface majority interacts magnetically with MFM probe. The observed contrasts clearly exhibit the existence of magnetic domains dispersed in the surface analyzed. A large number of uniform magnetic domains were seen in thickness δ between 10 nm and 100 nm (Fig. 9(a) and (b)). For $\delta = 10$ nm did show a significant contribution of magnetic moments on the surface, whilst films for $\delta = 100$ nm presented the single domains formation ranging in size 15 - 30 nm. At δ greater than 150 nm, the magnetic domains became larger. The domains were less distinct for $\delta = 400$ nm (Fig. 9(d)). This implies that there is a rise in the grains number that are in a magnetic multi-domain state. The magnetic structure change of Zr_6Co_{23}/MgO(001) film is the reason for the reduction of H_c and $(BH)_{max}$ for 400-nm film. Note that the average magnetic domain size is much larger than the average grain size. That is, one domain includes several grains, which is called an interaction domain [49]. This indicates the presence of a strong exchange coupling interaction between neighboring grains [50, 51]. The variation of the interaction domain size with thickness is attributed to the varied grain morphology and non-uniform grain size [52].

The magnetization curves M(H) of Zr_6Co_{23}/MgO(001) films as a function of δ thickness are given in Fig. 10. The determination of saturation magnetization M_s was performed using the following approximate expression [53–55]

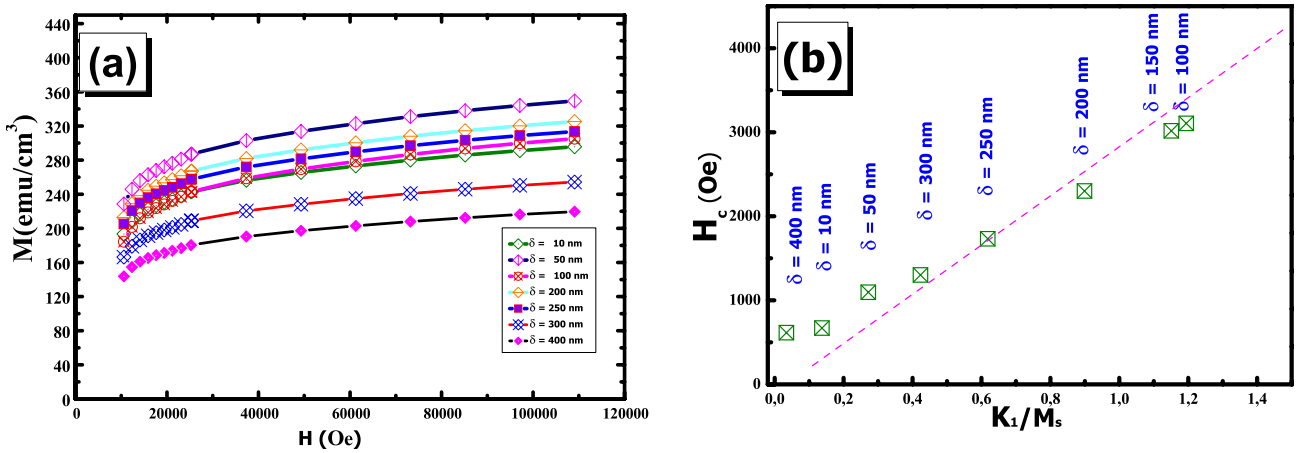

Fig. 10 **a** The magnetization curves M(H) of Zr_6Co_{23}/MgO(001) film as a function of δ thickness. **b** Variation of the experimental H_c data as a function of K_1/M_s. The magenta line represents the linear fit

$$M(H) = M_s + a/H^2 \quad (3)$$

H is the applied magnetic field. The coefficient is related to anisotropy field H_a, $a = -\frac{2}{105} H_a^2$. Expression (3) describes the magnetization approaching saturation in a system of randomly oriented particles with a cubic anisotropy [56]. The Zr_6Co_{23} compound has a cubic type crystal lattice in the nanocrystalline state. The magnetic moments in this compound are oriented toward several particular directions, so it has several easy magnetization axes (i.e., multiaxial) exhibiting a cubic anisotropy. The magnetization in a grain is supposed to be oriented in the same direction [2]. Each crystal grain has a cubic form in which the magnetic moment is uniformly distributed. The values of anisotropy constant K_1 have been calculated using the relation $K_1 = \frac{H_a M_s}{2}$. The saturation magnetization (M_s) increases from 249 emu/cm^3 at $\delta = 10$ nm to 327 emu/cm^3 at $\delta = 200$ nm, then decreases for $\delta > 200$ nm. The M_s decrease also leads to a decrease of K_1 from 1.35×10^7 erg/cm^3 to 0.18×10^7 erg/cm^3 (Table 6) and may be an additional reason for the disagreement on the thickness $\delta = 400$ nm. The squareness factor $S^* > 0.5$ indicates strong exchange interactions between the adjacent crystallites [57–60]. The H_c is correlated with M_s and K_1, which goes well with the Stoner Wohlfarth theory [43, 61]: $H_c = \alpha \frac{2K_1}{M_s} - N\frac{M_s}{\mu_0}$. $\alpha = f(a_k, a_j, a_{ex})$ and N are microstructural parameters. a_k, a_j, and a_{ex} coefficients are correlated consecutively with the grain sizes Φ and the pinning defect area and exchange interaction on the H_c. N is the demagnetization factor [43, 62]. Figure 10(b) presents the H_c experimental values as a function of $\frac{K_1}{M_s}$. H_c fits vary linearly with $\frac{K_1}{M_s}$ (purple line). The N value has been calculated to be around 2.23. The N value is not negligible. This confirms that the demagnetization impact is existent. The energy product $(BH)_{max}$ calculated for the 100-nm film from the M(H) curves, being about 28 MGOe. $(BH)_{max}$ is the maximum product of B and H for the B(H) demagnetization curve, where $B = H + 4\pi M$ and $H = H - N$. M are the magnetic field induction [63]. The S* value is 0.72 and $K_1 \simeq 1.35 \times 10^7$ erg/cm^3. These properties are important for technical interest and very promising for magnetic recording high density and spintronic applications. By comparing the results obtained for Zr_6Co_{23}/MgO(001) films with those found in the case of Zr_6Co_{23} films deposited on Al_2O_3 (0001) substrate by RF magnetron sputtering [11], it is observed in the second case that we have good quality films surfaces lead to values of H_c between 7916 Oe and 19352 Oe. The H_c values of the Zr_6Co_{23}/MgO(001) films are lower to those Zr_6Co_{23}/Al_2O_3 (0001) films. The K_1 values of Zr_6Co_{23}(100 nm)/MgO(001) and Zr_6Co_{23}(100 nm)/Al_2O_3 (0001) films are consecutively around 1.35×10^7 erg/cm^3 and 1.36×10^8 erg/cm^3. The magnetic anisotropy of Zr_6Co_{23} films is very sensitive to substrate nature, preparation conditions, surface roughness and intergrain exchange coupling.

Table 6 The value of M_s (emu/cm^3), $S^* = M_r/M_s$, H_a (Oe) and K_1($\times 10^7$ erg/cm^3) of nanocrystalline Zr_6Co_{23}/MgO(001) film for different δ thickness

δ(nm)	M_s	S*	H_a	K_1
10	249	0.77	61102	1.14
50	345	0.76	61131	1.16
100	306	0.72	61150	1.35
150	311	0.63	61202	1.33
200	327	0.67	61250	1.30
250	310	0.61	61161	1.27
300	248	0.58	60702	1.15
400	244	0.57	60033	0.18

4 Conclusion

Nanocrystalline Zr_6Co_{23} films of varying thickness δ were deposited by Pulsed Laser Deposition (PLD) on MgO(001) substrate. Grazing incidence X-ray diffraction (GIXRD) technique, atomic force microscopy (AFM) superconducting quantum interference device (SQUID), vibrating sample magnetometry (VSM) and magnetic force microscopy (MFM) were used to study the microstructural and magnetic properties of these films. The coercivity H_c, the squareness factor S* and the anisotropy field H_a were investigated as a function of δ thickness and grain sizes Φ. The coercivity H_c values are correlated with the saturation magnetization M_s and constant anisotropy K_1, which is consistent with the Stoner-Wohlfarth theory. The magnetic structure change of the Zr_6Co_{23}/MgO(001) film is the reason for the decrease in the magnetic anisotropy H_a and coercivity H_c as a function of δ. The excellent magnetic properties were found for $\delta =$ 100 nm: the coercivity $H_c = 3020$ Oe, maximum energy product $(BH)_{max}$ of 28 MGOe and magnetic anisotropy constant $K_1 = 1.35 \times 10^7$ erg/cm^3. The found results represent a fundamental reference for adapting the magnetic properties of Zr_6Co_{23}/MgO(001) films to potential applications in the field of permanent magnets.

Acknowledgements This work is main supported by the Romanian Ministry of Research and Innovation (Romania) and the "Ministère de l'Enseignement Supérieur et de la Recherche Scientifique" (Programme d'Encouragement des Jeunes Chercheurs (PEJC) - Session 2021 - Reference: 20PEJC 01-15) (Tunisia). The authors acknowledge the "Agence Universitaire de la Francophonie AUF" for his support.

References

1. Sharma, N., Jones, G.A., Casey, S.M., Grundy, P.J.: J. Phys. D: Appl. Phys. **31**, 3020 (1998)
2. Fersi, R., Bezergheanu, A., Patroic, D., Cizmas, C.B., Bessais, L., Mliki, N.: J. Magn. Magn. Mater. **494**, 165816 (2020)

3. Fersi, R., Bouzidi, W., Bezergheanu, A., Cizmas, C.B., Bessais, L., Mliki, N.: J. Magn. Magn. Mater. **451**, 473 (2018)
4. Bland, J.A.C., Heinrich, B.: Springer PP1, 65, 66, 67 (2005)
5. Fersi, R., Mliki, N., Bessais, L.: Magnetochemistry **8**(2), 20 (2022)
6. Yamkane, Z., Fersi, R., Rachid, F.Z., Moubah, R., Lassri, H., Mliki, N., Bessais, L.: J. Magn. Magn. Mater. 449 461 (2018)
7. Fõahler, S., Neu, V., Weisheit, M., Hannemann, U., Leinert, S., Singh, A., Kwon, A., Melcher, S., Holzapfel B., Schultz. L.: Proc. 18th Int. Workshop on High Performance Magnets and their Applications, **2**, 566 (2004)
8. Saito, T.: Mater. Trans. **44**, 1713 (2003)
9. Saito, T.: Appl. Phys. Lett. **82**, 2305 (2003)
10. Dalia, A.P., Fersi, R.: J. Magn. Magn. Mater. **532**, 167874 (2021)
11. Pareti, L., Solzi, M., Paoluzi, A.: J. Appl. Phys. **73**, 2941 (1993)
12. Binary Alloy Phase Diagrams, II Ed., Ed. T.B. Massalski, 2, 1264, H. Okamoto (1990)
13. Gabay, A.M., Zhang, Y., Hadjipanayis, G.C.: J. Magn. Magn. Mater. **236**, 37 (2001)
14. Saito, T.: Mater. Trans. **39** (No.5) 2890 (2003)
15. Stroink, G., Stadnik, Z.M., Viau, G., Dunlap, R.A.: J. Appl. Phys. **67**, 4963 (1990)
16. Hou, Z., Wang, W., Xu, S., Zhang, J., Wu, C., Su, F.: Phys. B: Cond. Matter. **407**, 1047 (2012)
17. Ishikawa, T., Ohmori, K.: IEEE Trans. Magn. **26**, 1370 (1990)
18. Burzo, E.: J. Appl. Phys. **70**, 6550 (1991)
19. Sakurai, M., Wu, S., Zhao, X., Nguyen, M.C., Wang, C.Z., Ho, K.M., Chelikowsky, J.R.: Phys. Rev. Materials **2**, 084410 (2018)
20. You, J., Guo, Y.: Mater. Lett. **241**, 84 (2019)
21. Bhardwaj, V., Prakash Pal, S., Rama Rao, N.V., Chatterjee R.: Mater. Lett. **260**, 126869 (2020)
22. Mitu, A., Dumitruc, M., Suvailaa, R., Opreaa, A., Gheorghea, I., Mereuta, P., Brajnicov, S., Burducea, I., Florea, N.M., Marginean, N., Glodariu, T., Dinescu, M., Danil, G.C.: Vacuum **161**, 162 (2019)
23. O'Hanlon J.F.: A User's Guide to Vacuum Technology. John Wiley and Sons. **385** (2015)
24. Dunlap, R.A., Small, D.A., MacKay, G.R., O'Brien, J.W., Dahn, J.R., Cheng, Z.H.: Can. J. Phys, **78**, 211 (2000)
25. Phejar, M., Paul-Boncour, V., Bessais, L.: Intermetallics. **18**, 2301–2307 (2010)
26. Rietveld, H.: J. Appl. Crystallogr. **2**, 65 (1969)
27. Rodrguez-Carvajal, J.: Physica B. **192**, 55 (1993)
28. Bessais, L., Fersi, R., Cabié, M., Mliki, N.: TMS2013 Supplemental Proceedings 97–104 (2013)
29. Fersi, R., Cabié, M., Mliki, N., Bessais, L.: Int. J. Hydrog. Energy. **44**, Issue 39 22011 (2019)
30. Jaballah, H., Bouzidi, W., Fersi, R., Mliki, N., Bessais, L.: J. Phys. Chem. **161**, 110438 (2022)
31. Yamkane, Z., Fersi, R., Rachid, F.Z., Moubah, R., Lassri, H., Mliki, N., Alleg, S., Sajieddine, M., Bessais, L.: SPIN, 2050016 (2020)
32. Servant, C., Guau, C., Ansara, I.J.: Alloys Compd. **220**, 19 (1995)
33. Svechnikov, V.N., Pan, V.M., Russ Spektor, A.T.: J. Inorg. Chem. **8**, 1106, 963 (2021)
34. Bakkari, K., Fersi, R., El Kebir, H., Bessais, L., Mliki, N.: J. Phys. Condens. Matter, **9**, 30 (2018)
35. Fersi, R., Mliki, N., Bessais, L.: IOP Conf. Series: Mater. Sci. Eng. **28**, 012014 (2012)
36. High Score software for crystallography, Philips analytical (2002)
37. Fersi, R., Mliki, N., Cabié, M., Bessais, L.: Phys. Status Solidi (a) **211**(4), 910 (2014)
38. Fersi, R., Mliki, N., Bessais, L., Guetari, R., Russier, V., Cabié, M.: J. Alloys Compd. **522**, 14 (2012)
39. Fersi, R., Cabié, M., Mliki, N., Bessais, L.: J. Alloys Compd. **576**, 415 (2013)
40. Fersi, R., Bouzidi, W., Mliki, N., Bessais, L.: Intermetallics **100**, 181 (2018)
41. Bessais, L., Fersi, R., Mliki, N.: TMS 2014: 143rd Annual Meeting & Exhibition, 2016, Springer International Publishing, Cham, 23-29 (2016)
42. Akhtar, M.S., Riaz, S., Mehmood, R.F., Ahmad, K.S., Alghamdi, Y., Azad Malik, M., Naseem, S.: Mater. Chem. Phys. **89**, 28 (2017)
43. Fersi, R., Jabbalah, H., Bezergheanu, A., Patroic, D., Cizmas, B., Bessais, L., Mliki, N.: Vacuum **174**, 109168 (2020)
44. Liu, Z., Yang, W., Li, M., Zhou, P., Yao, X., Chen, Y.: Ziyuan Hao IFAC-Papers OnLine **51**(17), 689 (2018)
45. Cullity, B.D., Wesley, A.: Reading. Mass, USA (1974)
46. George, M., John, A.M., Nair, S.S., Joy, P.A., Anantharaman, M.R.: J. Magn. Magn. Mater. **302**(1), 190 (2006)
47. Caizer, C.: Mater. Sci. Eng., B, **100**, 1 63 (2003)
48. Cheérif, S.M., Layadi, A., Ben Youssef, J., Nacereddine, C., Roussigne, Y.: Physica B. **387**, 281 (2007)
49. Woodcock, T.G., Khlopkov, K., Walther, A., Dempsey, N.M., Givord, D.: L. Schultz O. Gutfleisch. Scr. Mater. **60**, 826 (2009)
50. Dahal, J.N., Neupane, D., Mishra, S.R.: Ceramics **2**, 10 (2019)
51. Liang, Y., Deng, Q., Tan, X.H., Li, H., Xu, H.: Sci. Rep. **9**(1), 1758 (2019)
52. Huang, Y.L., Wang, Y., Hou, Y.H., Wang, Y.L., Wu, Y., Ma, S.C., Liu, Z.W., Zeng, D.C., Tian, Y., Xia, W.X. and Zhong, Z.C.: J. Magn. Magn. Mater. **399**, 175 (2016)
53. Chikazumi, S.: Physics of Ferromagnetism. 2nd ed. 672 p (2009)
54. Akulov, N.S.: Zeitschrift Phys. **69**, 822 (1931)
55. Komogortsev, V., Patrusheva, T.N., Balaev, D.A., Denisova, E.A., Ponomarenko, I.V.: Tech. Phys. Lett. **35**, 882 (2009)
56. Akulov, N.S., Kirensky, L.V., Tekh, Zh.: Fiz. **9**, 1145 (1939)
57. Fersi, R., Mliki, N., Bessais, L.: EPJ Web of Conferences **29**, 00018 (2012)
58. Bez, R., Fersi, R., Zehani, K., Moscovici, J., Bessais, L., Mliki, N., Fonda, E., Michalowicz, A.: J. Alloys Compd **666**, 317 (2016)
59. Fersi, R., Mliki, N., Bessais, L.: IOP Conf. Series Mater Sci Eng, **28**, 012014 (2012)
60. Fersi, R., Mliki, N., Bessais, L.: Supplemental Proceedings: Materials Properties. Characterization, and Modeling **1**, 863–869 (2012)
61. Long, E., Xiaoqiang, T., Lezhong, L., Rui, W.: J. Rare. Earth. **31**, 988 (2013)
62. Li, Y.F., Chen, D.X., Vázquez, M., Vázquez, M., Hernando, A.: J. Phys. D Appl. Phys. **35**(6), 508 (2002)
63. Balasubramanian, B., Das, B., Skomski, R., Zhang, W.Y., Sellmyer, D.J.: Adv. Mater. **25**, 6090–93 (2013)

Publisher's Note Springer Nature remains neutral with regard to jurisdictional claims in published maps and institutional affiliations.